



Trap passivation and suppressed electrochemical dynamics in perovskite solar cells with C₆₀ interlayers

Tulus^{a,b,†}, Loreta A. Muscarella^{c,d,†}, Yulia Galagan^{e,f,†}, Simon Christian Boehme^{a,§,†}, Elizabeth von Hauff^{a,g,h,*}

^a Department of Physics & Astronomy, Faculty of Sciences, Vrije Universiteit Amsterdam, 1081 HV Amsterdam, The Netherlands

^b Research Center for Advanced Materials, National Research and Innovation Agency (BRIN), Jakarta 10340, Indonesia

^c Center for Nanophotonics, AMOLF, Science Park 104, 1098 XG Amsterdam, The Netherlands

^d Department of Chemistry, Utrecht University, Princetonlaan 8, 3584 CB Utrecht, The Netherlands

^e TNO - Solliance, 5656 AE Eindhoven, The Netherlands

^f National Taiwan University, Department of Materials Science and Engineering, Taipei 106, Taiwan

^g Fraunhofer Institute for Organic Electronics, Electron Beam and Plasma Technology (FEP), Dresden, Germany

^h Faculty of Electrical and Computer Engineering, Technical University of Dresden, Dresden, Germany

ARTICLE INFO

Keywords:

C₆₀
ZnO
Transport layer
Perovskite
Impedance spectroscopy
Equivalent circuit model
Solar cell

ABSTRACT

In this study, we quantify the impact of C₆₀-passivation layers in Cs_{0.15}FA_{0.85}PbI_{2.75}Br_{0.25} double-cation perovskite solar cells. We apply a combination of impedance spectroscopy, photoluminescence (PL) spectroscopy, and X-ray diffraction (XRD) to identify the origin for the increase in power conversion efficiencies and operational stability for solar cells fabricated with C₆₀/ZnO electron transport layer (ETL) versus reference cells with a ZnO ETL. XRD reveals an increase in PbI₂ while PL spectroscopy reveals an increase in Br-rich regions in the perovskite bulk in devices containing C₆₀ interlayers. We apply impedance spectroscopy to quantify the electrochemical dynamics in both solar cell architectures. Solar cells with C₆₀/ZnO ETL demonstrate less pronounced and slower electrochemical dynamics in the impedance spectra than solar cells with ZnO ETL. We conclude that C₆₀ leads to the formation of PbI₂-rich and Br-rich domains in the perovskite absorber layer, resulting in reduced recombination losses and improved operational stability.

1. Introduction

Perovskite solar cells (PSCs) have attracted much attention in the last decade, following the pioneering application of methylammonium (MA) lead-halide perovskites in dye-sensitized solar cells in 2009 [1–3]. Since then, increases in efficiency have been achieved in planar, thin-film solar cell architectures using mixed cation and mixed anion perovskite absorber layers [4,5]. In light of the impressive improvements in performance witnessed in the last few years, the main challenge towards real applications is now to improve the operational stability and lifetime of PSCs [6–12]. Further optimization of PSCs is targeted by reducing charge trapping and surface recombination, through passivation of device interfaces, as well as improving bulk crystallinity and perovskite

stoichiometry [11,13,14]. The replacement of the volatile MA cation with other (inorganic) cations has further resulted in improved stability [15–18]. Double-cation mixed-anion perovskites such as Cs_xFA_{1-x}PbI_{3-y}(1-x)Br_y(1-x) (FA=formamidinium) have demonstrated promising results for achieving thermally stable perovskite layers [16,17,19–21]. Mixed I-Br halide perovskite absorber layers have resulted in improved performance [22]. This has been attributed to the superior stability as well as the larger bandgap due to the Br-rich content, which is correlated with higher open-circuit voltage (V_{oc}) [13,22]. In addition to perovskite composition, it has been recognized that electrical losses at the PSC interfaces are a crucial factor for improving perovskite solar cell performance and stability [10,13]. In this context, recent reports have highlighted the urgency to develop strategies to reduce interfacial

* Corresponding author at: Fraunhofer Institute for Organic Electronics Electron Beam and Plasma Technology: Fraunhofer-Institut für Organische Elektronik Elektronenstrahl- und Plasmatechnik FEP, Winterbergstr 28, Dresden, Germany

E-mail address: elizabeth.von.hauff@fep.fraunhofer.de (E. von Hauff).

† The authors declare no competing financial interest.

§ Present address Laboratory of Inorganic Chemistry, Department of Chemistry and Applied Biosciences, ETH Zürich, 8093 Zürich, Switzerland; Empa—Swiss Federal Laboratories for Materials Science and Technology, 8600 Dübendorf, Switzerland

recombination losses as well as prevent ion migration towards the device electrodes [10–14,23–25].

Metal oxides such as TiO_2 , SnO_2 and ZnO are obvious choices for the electron transport layer (ETL) in PSCs [10,26], as they are n-type materials with suitable energetics for electron extraction from the perovskite absorber, and can be processed at low temperature and cost [26]. Early work in the field of perovskite photovoltaics (PV) focused on TiO_2 ETLs, resulting in reasonable stability and performance [27]. However, ZnO may be a more suitable choice than TiO_2 , due to the combination of high electron mobility with low-temperature, flexible processing methods [26,28,29]. For example, mobility values of $205 - 300 \text{ cm}^2 \text{ V}^{-1} \text{ s}^{-1}$ have been reported for bulk ZnO [26,28,29] vs. $0.1 - 4 \text{ cm}^2 \text{ V}^{-1} \text{ s}^{-1}$ for bulk TiO_2 [29,30]. Further, the alignment of the conduction bands between ZnO and perovskite absorber layers for electron extraction reduces losses in carrier energy during extraction [26,28,31,32]. However, reports of decomposition of methylammonium lead-iodide (MAPbI_3), *i.e.* the first generation perovskite absorber layer, upon direct contact with ZnO (particularly after annealing) [28,33,34], resulted in less focus on ZnO ETLs in PSCs [26]. In addition, a major challenge associated with ZnO is the complex defect chemistry [28], which depends strongly on the fabrication process [28,35]. Miyasaka et. al., demonstrated ZnO -based triple-cation (Cs, FA, MA) perovskite PV yielding a power-conversion efficiency (PCE) of 18.9% [36], but in this study, low-temperature annealing of the perovskite layer was applied, which is not compatible with processes required for fabricating highly crystalline layers with reduced grain boundaries [36,37]. These challenges have inspired much research into strategies to improve the ZnO -perovskite interface [26,32,38]. Interface engineering using passivation layers has been applied to prevent non-radiative recombination losses due to defects at the contact interfaces, as well as preventing unwanted changes in the physical and chemical properties of the perovskite-contact interface [13,17]. Interface engineering with organic molecules, ranging from Lewis acids, to small molecules, to non-fullerene acceptors have been reported to increase the photoluminescence (PL) quantum yield of the perovskite absorber, correlated with decreased non-radiative recombination losses [13,17,37]. However, insulating passivation layers result in a drop in the cell potential at the contact and prevent the extraction of carriers from the device, and therefore the challenge is to develop chemically inert, conductive ETLs for PSCs [10]. Zheng et. al. demonstrated PSCs based on ZnS -passivated ZnO and a triple-cation perovskite absorber with good stability and a PCE of 20.7% [39]. Subsequent studies suggested that interfacial passivation with organic materials offers even greater potential to improve the quality and stability of ZnO /perovskite architectures [17,40–42]. For example, insulating polymeric buffer layers, such as polyethylene glycol (PEG) and polyethylenimine (PEI), have been used to passivate the ZnO ETL to achieve thermally stable cathode interfaces in PSCs [43]. C_{60} has good electron mobility and the LUMO level is suitably aligned with the ZnO conduction band, which, together, prevent potential difference losses at the contact interface [44]. The use of C_{60} passivation layers in PSCs has been widely investigated due to reports of increased photovoltaic performance, decreased hysteresis, and improved device stability [45–47]. While C_{60} has been associated with reduced ion migration and interfacial chemical reactions, the underlying physical and chemical mechanisms, in particular in combination with ZnO , leading to increased PSC performance are unknown [48].

In this study, we elucidate the origins for performance improvement in PSC containing C_{60} layers. We compare PSC containing C_{60}/ZnO ETLs with reference devices containing ZnO ETLs in the model system $\text{Cs}_{0.15}\text{FA}_{0.85}\text{PbI}_{2.75}\text{Br}_{0.25}$. We find that the C_{60} passivation layer results in higher V_{oc} and fill factors (FF), leading to higher PCE than devices without the C_{60} layer, consistent with previous reports [45–47]. Further, the C_{60} layer also decreases the hysteresis index and significantly improves the operational stability of the PSC [17,45,46]. We additionally observe a slight decrease in the short circuit current density (J_{sc}). Using a combination of photoluminescence (PL) spectroscopy and X-ray

diffraction (XRD), we show that perovskite/ C_{60} samples demonstrate a blue shift in the PL and the emergence of PbI_2 in the perovskite. This is consistent with the local formation of PbI_2 and Br-rich domains. We apply impedance spectroscopy (IS) to correlate the changes in PSC composition with photovoltaic performance. This allows us to quantify relevant dynamics, and relate this to PSC performance [49–53]. In this context, we apply a generalized equivalent-circuit model (ECM) for PSCs [53] to model the electronic and electrochemical dynamics [46,53–55]. Solar cells with a C_{60}/ZnO ETL demonstrate less pronounced electrochemical dynamics than solar cells with ZnO ETL. We conclude that the formation of PbI_2 and Br-rich domains improves PSC performance and operational stability through trap passivation and suppression of electrochemical degradation.

2. Results

2.1. The influence of C_{60} -interlayers on solar cell performance and stability

PSCs were fabricated with either ZnO or C_{60}/ZnO ETLs according to the procedure described in the methods section. Briefly, ZnO was spin-coated onto ITO substrates and then thermally annealed at 350°C for 20 min, using a previously published protocol [28,56]. For some samples, a thin layer of C_{60} was subsequently thermally evaporated on top of the ZnO . The perovskite absorber was spin-cast onto the ETL, and the devices were completed by spin-casting doped Spiro-OMeTAD and then subsequently thermally depositing Au electrodes (100 nm) to complete the stack.

Fig. 1 (a) and (b) show the SEM cross sections of the Spiro-OMeTAD/perovskite/ ZnO/ITO and the Spiro-OMeTAD/perovskite/ $\text{C}_{60}/\text{ZnO}/\text{ITO}$ structures, respectively. The thickness of ZnO is 55 nm, the thickness of C_{60} is 25 nm and the thickness of the perovskite is approximately 300 nm. For samples with the C_{60} interlayer, the morphology of the perovskite layer was visually smoother and with less grain boundaries, suggesting an improved crystal quality [57]. Fig. 1 (c) and (d) show the current-density - voltage (J-V) characteristics of freshly prepared champion cells with either a ZnO ETL or a C_{60}/ZnO ETL in the dark (black) and under illumination (blue), respectively; J-V characteristics of an aged sample under illumination is shown in red. The label “fresh” designates the first measurement on the sample prior to the stability test, while “aged” designates the measurement after 30 min from stability test without stress conditions in the dark. The J-V measurements were performed in reverse-scan configuration at a scan rate of 180 mV/s in the dark (black line) and under AM 1.5 standard illumination (red and blue lines). Fig. 1 (c) and (d) clearly illustrate the performance improvements enabled by the C_{60} interlayer: first, the series resistance is improved, yielding higher FF and PCE in freshly prepared sample. Second, and importantly, the stability is much improved; while the sample without C_{60} displayed strongly deteriorated diode characteristics after aging, suffering even complete break-down at reverse biases of -0.4 V (see Fig.1c), the sample with the C_{60} interlayer retains its superior diode characteristics even after aging (see Fig. 1d).

More specifically, the C_{60} interlayer improves the initial “fresh” solar cell performance, leading to an increase in PCE from 12.09% to 15.38%, due to an increase in the V_{oc} from 0.98 V to 1.04 V and in the FF from 64.39% to 77.23% in the champion cells. However, we observe a lower short-circuit current density (J_{sc}) ($19.21 \text{ mA}/\text{cm}^2$ versus $19.26 \text{ mA}/\text{cm}^2$) in the PSC with the C_{60} interlayer. More interestingly, the C_{60} interlayer improves the stability of the solar cell parameters: upon aging, the PCE decreases from 15.39% to 13.96% in the sample with the C_{60} interlayer, while the decrease is significantly larger, from 12.09% to 5.64%, in the sample without a C_{60} interlayer. We observe a similar trend in all solar cell parameters. In the device containing the C_{60} interlayer, the V_{oc} , FF, and J_{sc} decrease from 1.04 V to 1.02 V, from 77.23% to 72.74%, and from $19.21 \text{ mA}/\text{cm}^2$ to $18.74 \text{ mA}/\text{cm}^2$, respectively. In contrast, the V_{oc} significantly decreases from 0.98 V to 0.82 V, the FF from 64.39% to

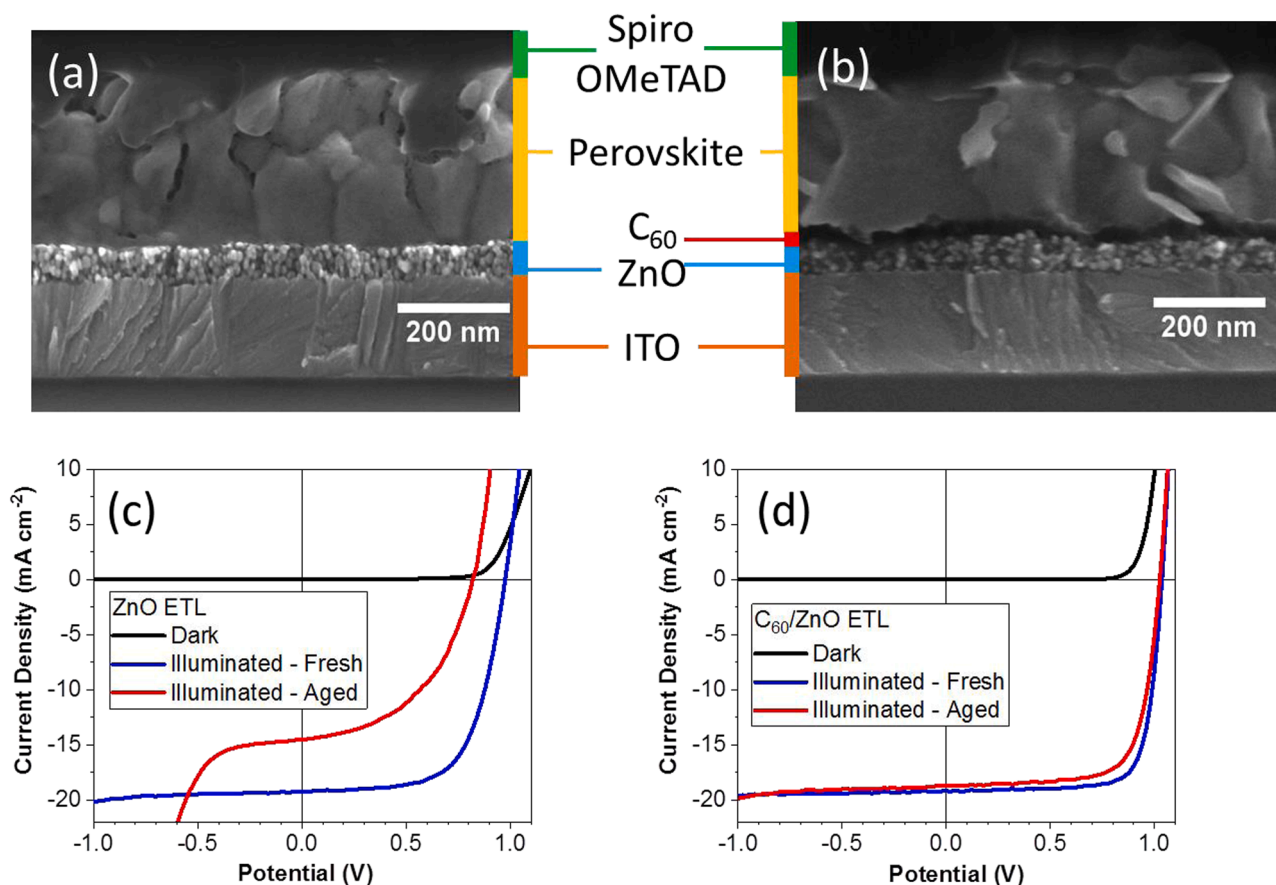


Fig. 1. (a) and (b) The SEM cross-section images of the Spiro-OMeTAD/perovskite/ZnO/ITO and the Spiro-OMeTAD/perovskite/C₆₀/ZnO/ITO structures, respectively. The J-V characteristics of champion cells for the (c) PSC with the ZnO ETL and the (d) PSC with the C₆₀/ZnO ETL in the dark (black), under AM1.5 illumination on the fresh (blue) and aged (red) samples, respectively.

47.26%, and the J_{sc} from 19.26 mA/cm² to 14.52 mA/cm² in the device without C₆₀ interlayer. The hysteresis index is also lower in the devices containing the C₆₀ layer, consistent with previous reports (see supplementary information in Figure S1c) [45,46,47]. The solar cell parameters of the champion cells (fresh and aged) are summarized in Table 1.

Fig. 2 shows the distribution in the values of (a) PCE, (b) J_{sc} , (c) V_{oc} and (d) FF for 21 PSC devices either with the ZnO ETL (red) or with the C₆₀/ZnO ETL (blue), obtained from J-V scans in reverse-scan direction. A total of 21 samples were measured for each device architecture. On average, addition of the C₆₀ interlayer leads to an increase in PCE from 11.68 ± 2.51 % to 13.02 ± 2.93 %, in V_{oc} from 0.99 ± 0.05 V to 1.03 ± 0.03 V, and in FF from 61.69 ± 6.34 % to 72.00 ± 5.95 %. However, we note a slight decrease in J_{sc} from 19.19 ± 0.99 mA/cm² to 18.92 ± 1.47 mA/cm² in devices with C₆₀/ZnO ETLs compared to devices prepared with ZnO ETLs.

Fig. 3 shows the device stability under constant AM 1.5 illumination, reporting over 1000 min the evolution of the normalized (a) PCE, (b) J_{sc} , (c) V_{oc} , and (d) FF. The PCE of the device with the C₆₀/ZnO ETL decreases to 84 % of the initial value, while the PCE of the device with the ZnO ETL

Table 1

Parameters from champion cells (fresh and aged) with the ZnO ETL and with the C₆₀/ZnO ETL in the dark and under AM 1.5 standard illumination.

Sample Name	Sample Condition	J_{sc} (mA cm ⁻²)	V_{oc} (V)	FF (%)	PCE (%)
PSC with ZnO ETL	Fresh	19.26	0.98	64.39	12.09
	Aged	14.52	0.82	47.26	5.64
PSC with C ₆₀ /ZnO ETL	Fresh	19.21	1.04	77.23	15.38
	Aged	18.74	1.02	72.74	13.96

decreases to 44 % of the initial value under the same stress conditions. These results are consistent with previous reports that have shown C₆₀ ETL interlayers to enhance perovskite solar cell stability [45]. The PSC with the ZnO ETL shows a rapid burn-in followed by slower degradation, while the PSC with the C₆₀/ZnO ETL exhibits slow degradation without pronounced burn-in. Burn-in is well-documented in PSC but the exact mechanism are unknown [58,59]. We find that the improved stability of the PSC with the C₆₀ layers can be traced back to well-sustained charge generation and collection, inferred from the stable J_{sc} (see Fig. 3b), and to the lack of formation of non-radiative loss channels, as inferred from the constant V_{oc} (see Fig. 3c).

We extracted the saturation current (J_0), the series resistance (R_s) and the shunt resistance (R_{SH}) from the J-V curves (see methods section for details). Fig. 4 show the change in (a) J_0 , (b) R_s , and (c) R_{SH} , during the stability test. Compared to the devices with the ZnO ETL (red), the devices with ZnO/C₆₀ ETL (blue) consistently exhibit a lower J_0 , lower R_s , and higher R_{SH} . The decrease in R_s indicates less electrical losses at device contacts, while the increase in R_{SH} correlates with improved current rectification in the dark J-V characteristics (see also Fig. 1).

Further, the J_0 values increase significantly over time in the sample with the ZnO ETL, while J_0 values are relatively stable over time in the PSC with the C₆₀/ZnO ETL. A similar trend is observed in the R_s values. Finally, the C₆₀ layer leads to higher R_{SH} values than in PSC with ZnO ETL.

2.2. The influence of C₆₀ on the perovskite-ETL interface

To gain more insight into the impact of the C₆₀ interlayer on the quality of the perovskite-ETL interface, we performed PL spectroscopy

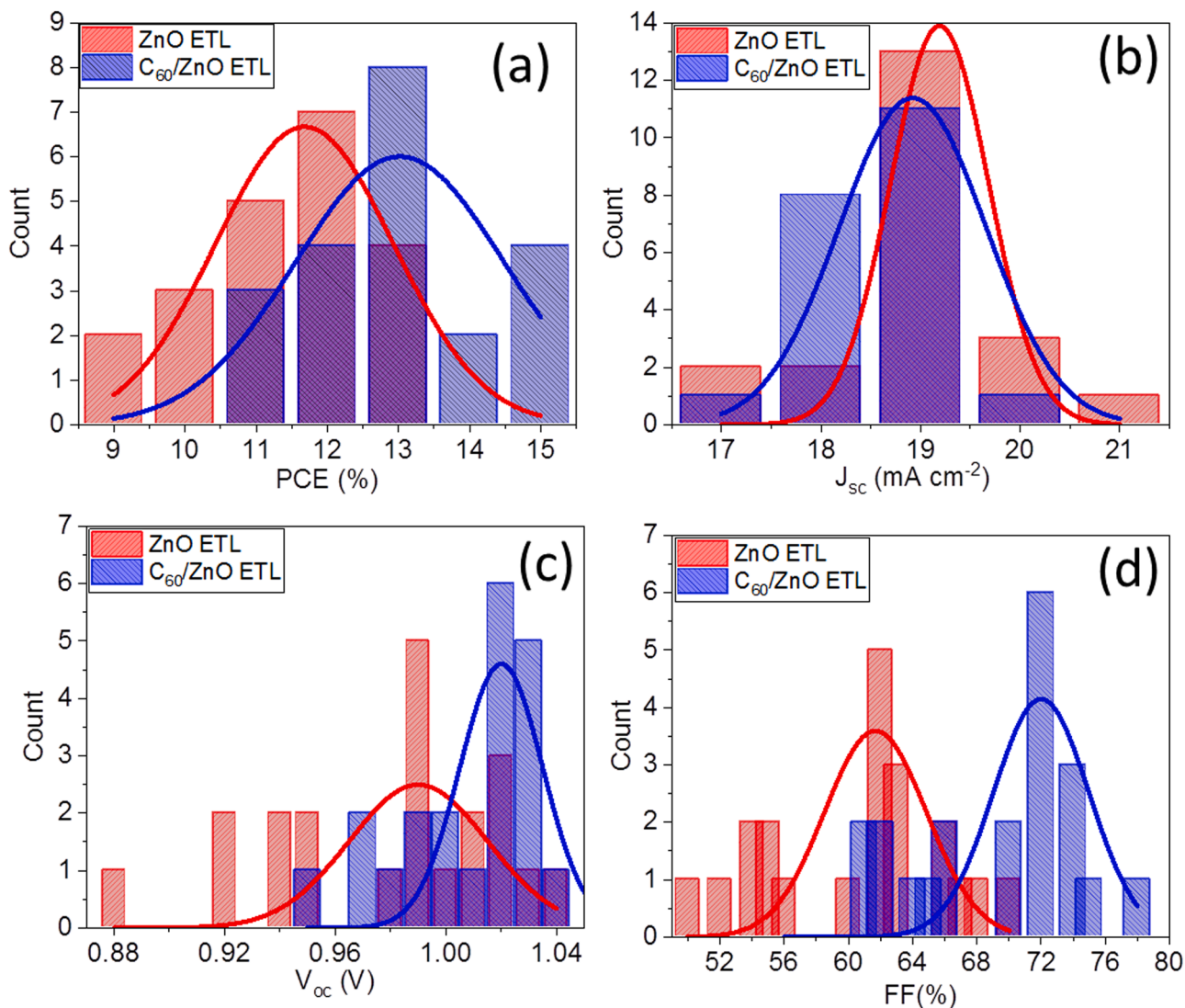


Fig. 2. Distribution of solar cell parameters (a) PCE, (b) J_{sc} , (c) V_{oc} and (d) FF prepared with C_{60}/ZnO ETLs (blue) and ZnO ETLs (red), respectively. A total of 21 samples were measured for each device architecture.

and XRD experiments. Fig. 5 shows the PL spectra of three different layer stacks on glass substrates, i.e. a simple perovskite thin film (black), a perovskite/ZnO stack (red), and a perovskite/ C_{60}/ZnO stack (blue), respectively. The samples were excited at 2.64 eV and the PL spectra were obtained either under front illumination (FI), i.e. the perovskite layer faces both excitation source and PL detector, or under back illumination (BI), i.e. both the excitation light and the collected perovskite PL pass through the glass substrate at the back of the sample.

The PL signal is highest for the perovskite-only layer, while perovskite layers interfaced with the ETLs show PL quenching. This is consistent with previous reports suggesting non-radiative recombination losses at the PSC ETL [46]. Interestingly, however, we note that the PL signal is significantly higher in the perovskite/ZnO structure compared to that of the perovskite/ C_{60}/ZnO structure. Since the absorbance of both stacks is quasi-identical (see Figure S7), we exclude photon-propagating effects such as absorption and reflection of excitation or emission light as the origin for the observed differences in PL quenching. Likewise, strong PL quenching in the perovskite/ C_{60}/ZnO stack is inconsistent with the C_{60} -mediated passivation of interfacial losses, as suggested by the PSC data in Fig. 2. Furthermore, we observe that the PL peak of the perovskite/ C_{60}/ZnO structure (1.58 eV) is blue-shifted compared to the peak of the perovskite/ZnO structure (1.57 eV). This may be an indication of the formation of the Br-rich wider

bandgap perovskite [17]. We also note spectral asymmetry in the PL of the perovskite/ C_{60}/ZnO structure for spectra recorded via back illumination (see Figure S8). This may indicate phase segregation that perhaps leads to the formation of Br-rich and I-rich domains at the device interfaces, known to correlate with solar cell stability [60–62].

To investigate this further, we performed XRD. Fig. 6 shows the XRD pattern of perovskites/ZnO/ITO (red), and perovskites/ C_{60}/ZnO /ITO (blue) on glass substrates, respectively. The characteristic perovskite peaks were observed at 14.03° (001), 19.85° (011), 24.42° (111), 28.25° (002), 31.61° (012), 35.22° (112), 40.33° (022), and 42.94° (003), respectively [5,15,63,64]; the peaks labelled with an asterisk (*) are attributed to the ITO substrate [28]. While we cannot distinguish whether the perovskite is I-rich or Br-rich, the XRD pattern of the perovskite/ C_{60}/ZnO /ITO structure indicates the formation of PbI_2 , inferred from the peak at 12.63° [5]. Since no major PbI_2 content is detected in the perovskite/ZnO/ITO structure, it is conceivable that there is a causal relationship between the appearance of the PbI_2 and the decreased PL in the C_{60} -containing sample [10,22,57]. Together, the PL and XRD results confirm the positive impact of C_{60} on the structural and opto-electronic properties of the PSC/ETL interface [10,22,57]. Interestingly, however, the non-radiative recombination losses are higher in the perovskite/ C_{60}/ZnO structures, which may correlate with the lower J_{sc} values in PSCs with C_{60}/ZnO ETLs, possibly related to the conversion of

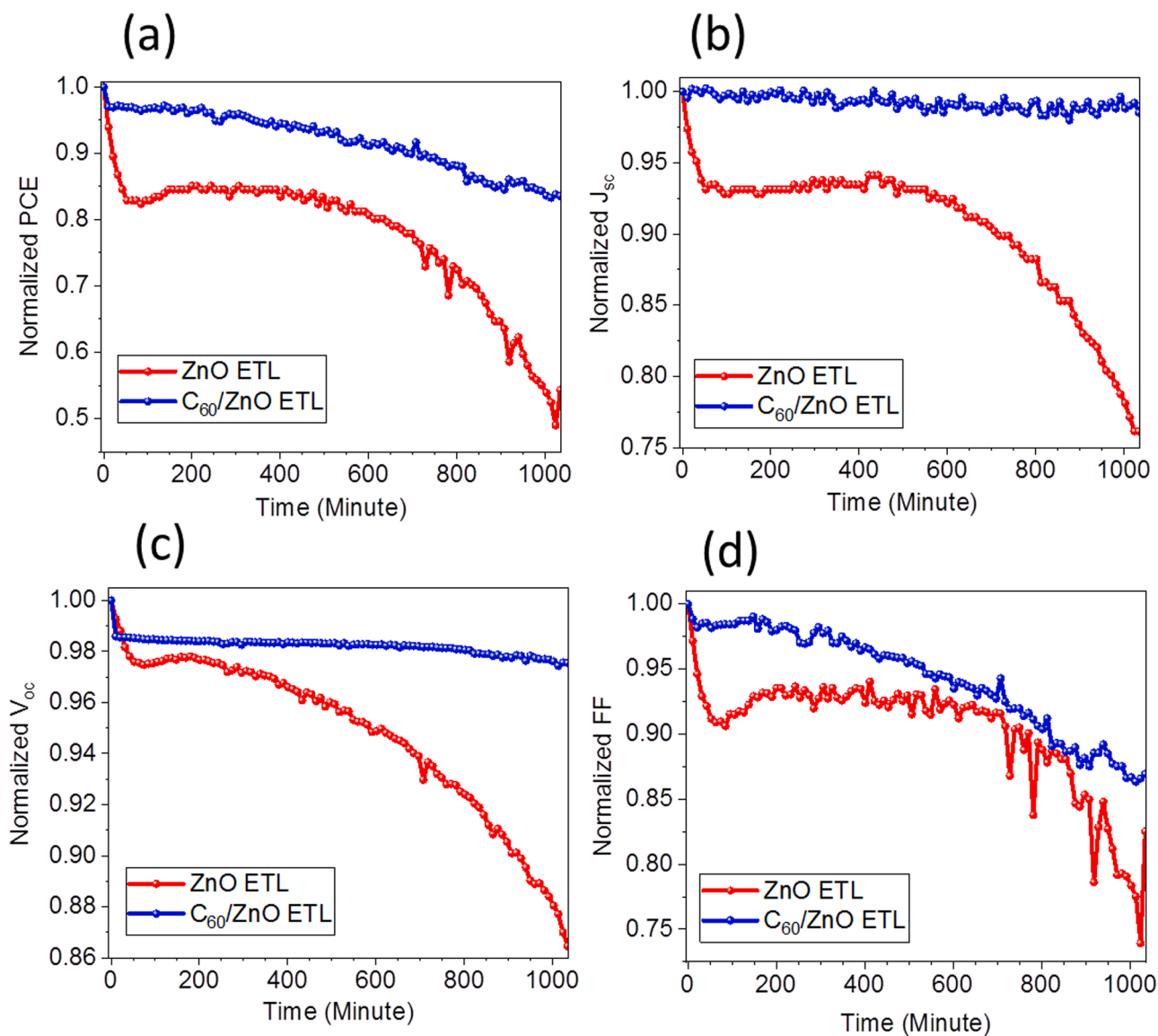


Fig. 3. The change in the solar cell parameters (normalized), (a) PCE (b) J_{sc} (c) V_{oc} (d) FF during constant AM 1.5 illumination of PSC devices with the ZnO ETL (red), and with the C₆₀/ZnO (blue) ETL, respectively.

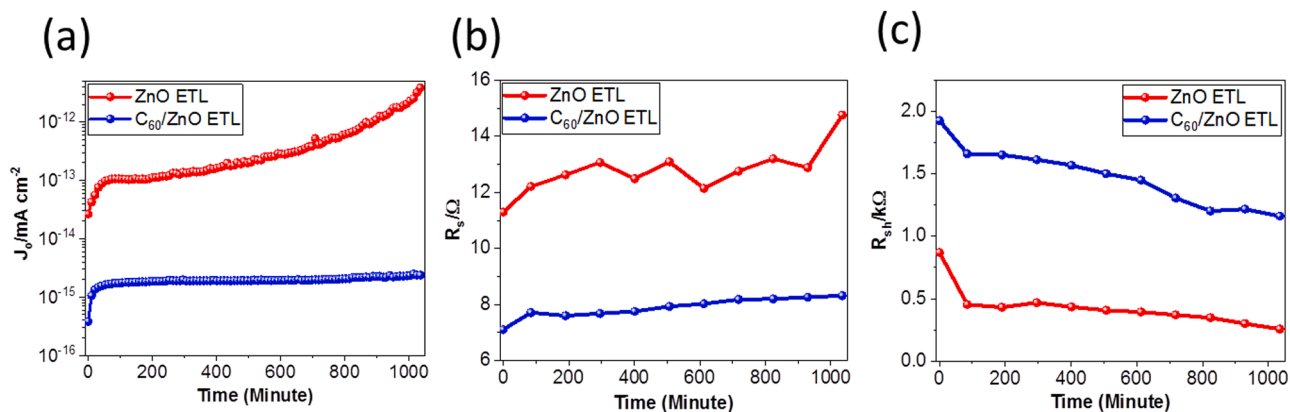


Fig. 4. (a) J₀, (b) R_s, and (c) R_{sh} versus time under constant AM 1.5 illumination for the PSC with ZnO ETL (red) and C₆₀/ZnO ETL (blue), respectively.

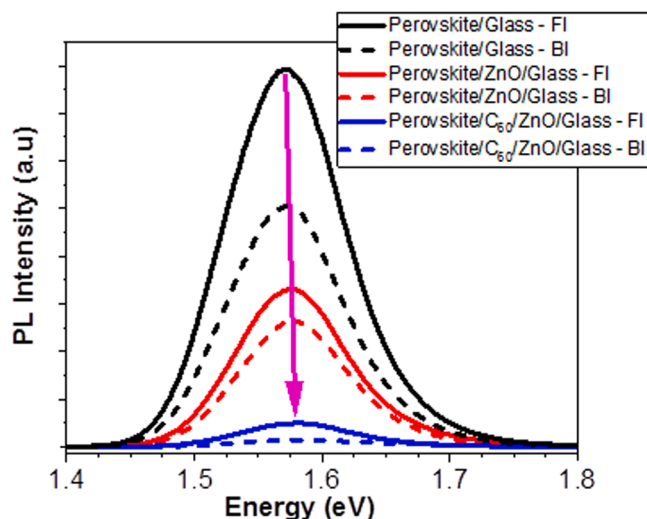


Fig. 5. PL spectra of a perovskite layer (black), a perovskite/ZnO stack (red), and a perovskite/ C_{60} /ZnO stack (blue) on glass substrates, obtained either via front illumination (FI, solid lines) or back illumination (BI, dashed lines).

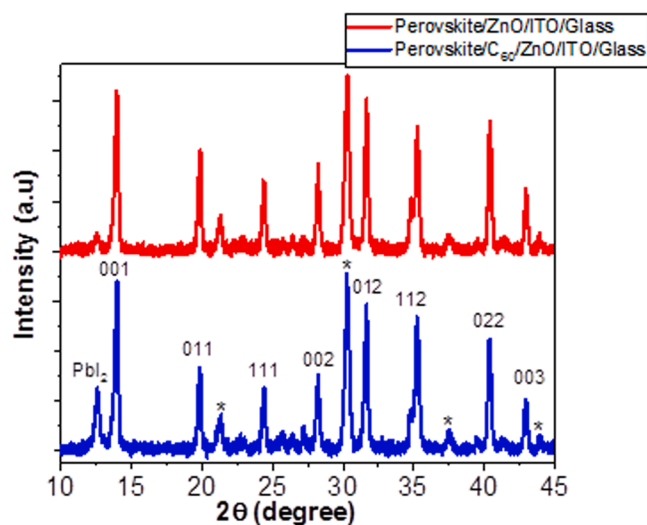


Fig. 6. XRD pattern of perovskite/ZnO/ITO (red) and perovskite/ C_{60} /ZnO/ITO (blue) structures on glass substrates. The peaks labelled with an asterisk (*) originate from the ITO substrate.

photo-active perovskite into insulating PbI_2 [17,57]. On the other hand, the formation of PbI_2 may stabilize grain boundaries and interfaces, thereby contributing to the increased device stability (see Figs. 3 and 4) [57].

Next, we applied IS to quantify the electrochemical dynamics at the ETL interface [49,53]. It was recently shown that the impedance spectra from PSCs can be modelled with a generalized ECM that accounts for fast electrical dynamics resulting in high frequency (HF) signatures, and much slower electrochemical dynamics that result in low frequency (LF) signatures [53]. The linear circuit is appropriate because the HF and LF signatures are separated in the frequency domain by several orders of magnitude. While LF signatures are ubiquitous to IS on PSCs, the form of the signature varies between cell architectures, as these depend on the nature of the electrochemical process in the device, i.e. ionic transport or a chemical reaction. Therefore, the analysis of the LF signature can be very insightful in order to understand specific loss mechanisms in different PSC architectures.

The IS data was measured under illumination at an applied DC po-

tential difference offset of 0.9 V (close to V_{oc}). IS was performed at V_{oc} , as this operational point results in the most reliable and stable spectra, and yields data that are relevant for both performance and stability. Fig. 7 shows the Nyquist plots of the experimental data (blue) and the ECM fits (red) for PSCs fabricated with either (a) ZnO, or (b) C_{60} /ZnO ETL, respectively. The ECM used here consists of a series resistance R_0 to account for parasitic resistances at the device contacts, a capacitor-resistor (RC) element to model fast electronic dynamics, and an RC element to describe slow electrochemical processes. We modified the generalized ECM to include constant-phase elements (CPEs) instead of capacitors in the RC elements to account for possible time dependence (dispersion) in the relaxation times of the dynamics related to inhomogeneity in the sample [49]. The impedance of the CPE (Z_{CPE}) is given by

$$Z_{CPE} = \frac{1}{Q(i\omega)^\alpha} \quad (1)$$

where ω is the angular frequency, Q is a coefficient and α is a unit-less parameter between 0 and 1 that accounts for dispersion in the system. If $\alpha = 1$, CPE reduces to an ideal capacitor with $Q = C$, and if $\alpha = 0$, the CPE reduces to an ideal resistor with $Q = 1/R$.

The time constant (τ) of the relaxation process is given by

$$\tau = \alpha\sqrt{R\cdot Q} \quad (2)$$

where, for $\alpha=1$, the time constant is given as $\tau = R\cdot C$ [55].

While the generalized ECM (R_0 , R_1 - Q_1 , and R_2 - Q_2) allows for a good fit to the IS data of the PSC with the C_{60} /ZnO ETL (see Fig. 7b), the fit quality is reduced for the case of the PSC with the ZnO ETL, and one RQ element (R_2 - Q_2) is not sufficient to model the dominant LF signature. Therefore, we expanded the LF component of the ECM (Fig. 7 a) to include two RQ elements, R_2 - Q_2 and R_3 - Q_3 . The difference in the LF signature between the two PSC architectures indicates that the C_{60} layer impacts either the nature of the electrochemical processes at the ETL and/or their timescales. The values of the circuit elements from the ECM for both device architectures are summarized in Table 2. We discuss the physical interpretation of these circuit elements in more detail below.

R_0 corresponds to the series resistance (R_{series}) that arises due to parasitic losses at the contacts. We compared the values of R_{series} extracted from the ECM to the values for the series resistance extracted from the J-V curve (see Fig. 4b), and find that these values agree well. For the PSC with the ZnO ETL, we find R_{series} values of 9.47 Ω and 11.29 Ω for the ECM and J-V data, respectively. For the PSC with the C_{60} /ZnO ETL, we find R_{series} values of 5.45 Ω (ECM) and 7.11 Ω (J-V curve). We note that the decrease in R_{series} in the PSC with C_{60} /ZnO ETL corresponds to an increase in the FF, indicating that the C_{60} layer facilitates efficient carrier extraction from the PSC.

The R_1 - Q_1 element corresponds to fast electrical (HF) dynamics in the PSC, while the R_2 - Q_2 (and R_3 - Q_3) element(s) correspond to the slow electrochemical (LF) dynamics in the PSC. It has already been reported in several studies that the fast electrical and slow electrochemical dynamics are interdependent, as ion rearrangement results in a change in the electrostatic environment, thereby impacting electrical transport in the PSC [53–55]. However, it has been shown that because the HF and LF dynamics are separated by several orders of magnitude in frequency, they can be independently modelled in a linear ECM [53].

It was shown that the geometric capacitance (C_{geo}) of the PSC dominates the HF signature, resulting in a slowing and a merging of all HF transport and recombination dynamics into a single relaxation in the Nyquist plot [53]. Therefore, the HF R_1 - Q_1 element models the cumulative electrical dynamics (transport and recombination) in the PSC. We find that Q_1 is comparable between the PSC with ZnO and the PSC with C_{60} /ZnO ETL (81.39 nF and 74.04 nF, respectively) while α_1 is close to one in both cases (0.88 and 0.93, respectively), indicating that Q_1 has nearly ideal capacitive character, and that the C_{60} layer has minimal impact on this parameter. Therefore, we propose that Q_1 approximates

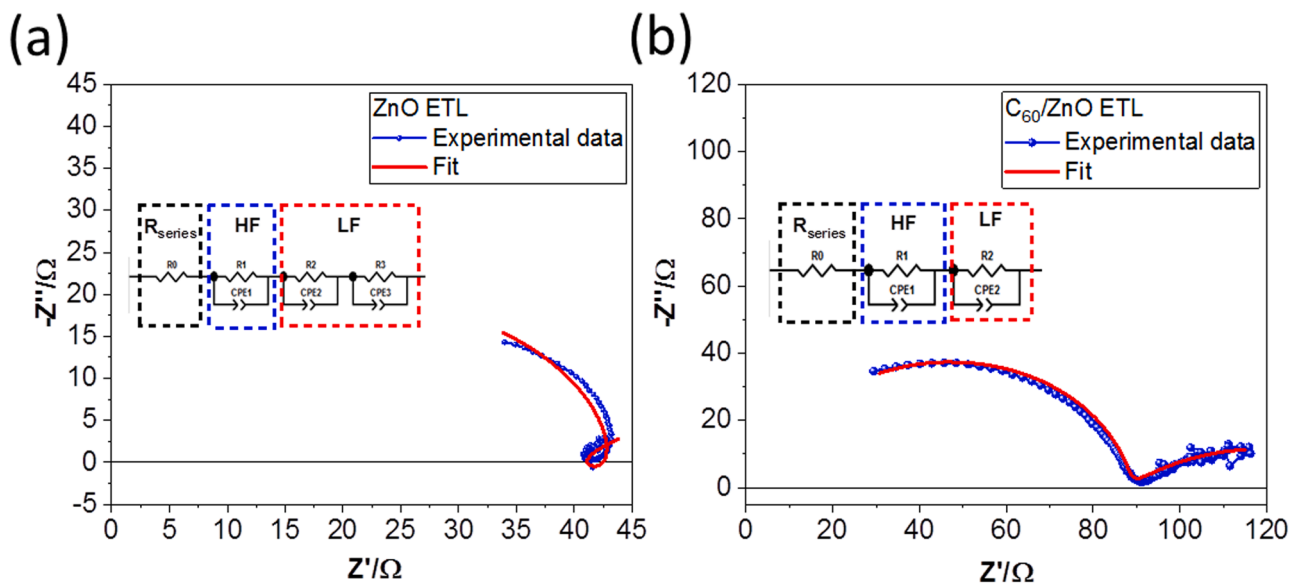


Fig. 7. Nyquist plots with experimental data (blue symbols) and fits using the generalized ECM (red lines) for a PSC with (a) a ZnO and (b) a C_{60}/ZnO ETL. The IS data was measured under illumination at a DC offset of 0.9 V. The insets show the employed ECM.

Table 2

Parameters extracted from the fits using the generalized ECM for PSCs with the ZnO (R_0 , R_1 - Q_1 , R_2 - Q_2 and R_3 - Q_3) and C_{60}/ZnO ETL (R_0 , R_1 - Q_1 , and R_2 - Q_2), respectively.

Sample Name	R_0 (Ω)	R_1 (Ω)	Q_1 (nF)	α_1	τ_1 (μ s)	R_2 (k Ω)	Q_2 (mF)	α_2	τ_2 (s)	R_3 (k Ω)	Q_3 (mF)	α_3	τ_3 (s)
PSC with ZnO ETL	9.47	49.75	81.39	0.88	0.69	-5.47	-2.59	0.11	6.84×10^{10}	17.84	2.79	0.11	8.33×10^{14}
	R_0 (Ω)	R_1 (Ω)	Q_1 (nF)	α_1	τ_1 (μ s)	R_2 (Ω)	Q_2 (mF)	α_2	τ_2 (ms)				
PSC with C_{60}/ZnO ETL	5.45	82.43	74.04	0.93	2.59	62.11	8.85	0.45	264.65				

C_{geo} very well. R_1 is an effective electrical resistance that models the (change) in transport and recombination processes. We observe that the R_1 is larger in the PSC with C_{60}/ZnO ETL (82.43 Ω) than the PSC with ZnO ETL (49.75 Ω). Generally, an increase in R_1 may be attributed to increased recombination losses (increase in recombination resistance), a decrease in photoconductivity (lower photocurrent), and/or a voltage drop in the PSC with C_{60} interlayers due to the relatively low carrier mobility in C_{60} compared to the perovskite and ZnO layers, and/or insulating PbI_2 domains in the active layer. From the J-V characteristics, however, we observe that the C_{60} layer leads to an increase in both V_{oc} and FF, which correlates with a decrease in recombination losses and does not indicate any voltage losses in the PSC. The PSC with C_{60}/ZnO ETL additionally demonstrate higher shunt resistances (see Table S1), which is consistent with reduced recombination and increased V_{oc} . We do observe a slight loss in J_{sc} due to the increase in the perovskite bandgap, which is correlated with lower carrier density. Therefore, the larger R_1 observed in the PSC with C_{60}/ZnO ETL may be due to the lower photocurrent density in these devices. The increase in R_1 in PSC with C_{60}/ZnO ETL is correlated with an increase in the effective relaxation time τ_1 from 0.69 μ s to 2.59 μ s. However, since the HF dynamics are limited by the geometric capacitance of the PSC, it is not possible to assign τ_1 to specific electrical processes in the PSC.

The HF signatures are associated with electrical transport and recombination processes and are therefore comparable between PSC. In contrast, the LF signature arises due to electrochemical dynamics that are highly sample-specific. Here we observe that the LF signatures show markedly more pronounced differences between the PSC architectures than the HF signatures. Specifically, two RQ (R_2 - Q_2 and R_3 - Q_3) elements were required to model the LF signature in the PSC with the ZnO ETL, in contrast to one RQ (R_2 - Q_2) element for the PSC with the C_{60}/ZnO ETL. Further, in the case of the PSC with the ZnO ETL, we observe that both α_2 and α_3 are much smaller than 1, which indicates highly dispersive

dynamics. The very long timescales τ_2 and τ_3 (10^{10} - 10^{14} s) suggest very slow and/or irreversible processes, such as mass transport or chemical reactions. The inductive nature of the LF signature arises when the current signal from the IS measurement leads the voltage excitation, which has been attributed to the interaction of ionic species with trap states [53].

In contrast, the PSC with the C_{60}/ZnO ETL demonstrates a less pronounced LF signature with faster timescales, on the order of ms. There is evidence of dispersion, i.e. α is 0.45, consistent with a mix of conductivity and capacitance. This behavior is consistent with reversible processes, such as ion-induced trap passivation [53]. In combination with the difference in burn-in trends observed in the solar cell parameters (Fig. 3), the IS analysis strongly suggests that the C_{60} layer suppresses irreversible electrochemical dynamics at the ETL interface.

3. Discussion

The C_{60} layer increases the V_{oc} and FF, and therefore the power conversion efficiency of the solar cells, indicating reduced recombination losses at the ETL/perovskite interface [13,17,37]. Additionally, the C_{60} layer improves the operational stability of the PSC.

We attribute the improvement in PSC performance and stability to microscopic segregation of the PSC into PbI_2 -rich and Br-rich domains, as observed in the PL (Fig. 5) and the XRD (Fig. 6), respectively. In the context of the device performance, local segregation of the perovskite into PbI_2 and Br-rich domains is consistent with the slight decrease in J_{sc} resulting from reduced light absorption in the PbI_2 and Br-rich domains. While an increase in the bandgap is correlated with increased V_{oc} , excess PbI_2 has been associated with reduced defects at surface, interfaces, and grain boundaries, as well as improved operational stability [17,48,57].

Based on these results, we propose that C_{60} layers increase PSC efficiency and stability by promoting the local formation of PbI_2 and Br-

rich domains, leading to (1) passivation of interfacial trap states, (2) increase in bandgap and therefore V_{oc} , (3) reduction in I_2 dissociation and I diffusion over time, and/or (4) reduction of slow Br-I segregation [17,21,31,37,65]. The passivation of interfacial states and increased bandgap are correlated with increased FF and V_{oc} . This effect compensates slight losses in J_{sc} due to the wider bandgap. More significantly, the reduction in electrochemical degradation (as evidenced by the suppression of the electrochemical dynamics in the IS) correlates with more stable solar cell parameters, i.e. a decrease in solar cell burn-in.

4. Conclusions

We systematically investigate the impact of C_{60} interlayers on PSC performance and stability using a combination of J-V, IS, PL and XRD. We observe that PSCs with C_{60}/ZnO ETL demonstrate higher FF and V_{oc} and better operational stability and less burn-in than PSCs with a ZnO ETL. We correlate this improved performance to segregation of the perovskite layer. The XRD and PL reveal that the C_{60} layer leads to an increase in PbI_2 as well as an increase in Br-rich PSC, correlating to a slight decrease in the J_{sc} in PSC with C_{60}/ZnO ETLs. We applied a general ECM to analyse the IS data from both PSC structures and show that the C_{60} interlayers suppress the electrochemical dynamics.

5. Experimental section

5.1. Materials

Zinc acetate dihydrate (analysis grade) was purchased from Merck Chemicals and used as received. Cesium iodide (CsI), Spiro-OMeTAD (HPLC grade, purity 99%), Bis (trifluoromethane) sulfonimide lithium, Chlorobenzene, Ethanolamine (ACS reagent grade, purity >99%), N,N-Dimethylformamide/DMF, Dimethyl sulfoxide/DMSO, 4-Tert-butylpyridine (purity 96%), Acetonitrile, Acetone were purchased from Sigma Aldrich and used as received. Formamidinium Iodide/FAI (purity 99.99 %) was purchased from Greatcell Solar (formerly Dyesol). Lead(II) Iodide/ PbI_2 (purity 99.99 %), Lead(II) Bromide/ $PbBr_2$ (purity > 98 %) were purchased from TCI. Ethanol (absolute) was purchased from VWR CHEMICALS. C_{60} (99.5%) was purchased from Solene.B.V and used as received. Au (purity 99.99%) was purchased from Cookson Drijfhout B. V.

5.2. Synthesis of ZnO nanostructure by a sol-gel process

ZnO seed layers were prepared using a sol-gel method on ITO sputtered glass substrates (Prazisions Glas & Optic GmbH) with a size of $(25 \pm 0.5) \text{ mm} \times (25 \pm 0.5) \text{ mm}$ and a thickness of $(1.1 \pm 0.1) \text{ mm}$. ITO substrates were cleaned for 15 min in acetone, then 15 min in ethanol, and finally 15 min in milli-Q water ($18 \text{ M}\Omega \text{ cm}$). All cleaning steps were performed in an ultrasonic bath at room temperature. Finally, the substrates were dried under nitrogen and subsequently exposed to UV/ozone (ProCleaner 220, Bioforce Nanoscience Inc.) for 15 min. For the fabrication of ZnO seeds, solutions with concentrations of 0.5 M of zinc acetate dihydrate and ethanolamine with a molar ratio of 1:1 in ethanol were used. The mixture was put in an ultrasonic bath at 40°C for 20 min and was kept stirring at 40°C for an additional 20 min. This step was repeated until a clear solution was obtained. The precursor solution was then allowed to cool to room temperature and 200 μL of this solution was subsequently deposited on ITO glass substrate by spin-coating at 2000 rpm for 30 s. The obtained film was thermally annealed using a precision hot plate at 350°C for 20 min in air.

5.3. Deposition of C_{60} on ZnO

C_{60} was deposited on ZnO in a thermal evaporation chamber at 1×10^{-6} mbar at a source temperature of 450°C . The sample was kept at room temperature. The recorded thickness of the C_{60} layer was 25 nm.

5.4. Preparation of mixed-cation and mixed-halide lead perovskite layers

The perovskites ($\text{Cs}_{0.15}\text{FA}_{0.85}\text{PbI}_{2.75}\text{Br}_{0.25}$) were prepared using 760 mg of CsI, 2850 mg of FAI, 8259 mg of PbI_2 , and 895 mg of PbBr_2 in 13.5 mL of DMF and 1.5 mL of DMSO. The solutions were stirred at room temperature for few hours in an N_2 environment. A film was deposited by spincoating 60 μL of the solution on top of either ZnO or C_{60}/ZnO at 6000 rpm for 60 s. 25 s after start of the spincoating process, 210 μL of chlorobenzene was sprayed on the films. The obtained films were thermally annealed at 100°C for 30 min in an N_2 environment.

5.5. Deposition of doped Spiro-OMeTAD as the hole-transport layer

80 mg of Spiro-OMeTAD was dissolved in 1 ml of chlorobenzene. The solution was then stirred overnight. 28.5 μL 4-tert-butyl pyridine, followed by 17.5 μL of lithium bis(trifluoromethane)sulphonimide solution (520 mg lithium bis(trifluoromethane)sulphonimide /1 ml acetonitrile) were then added to the solution. The solution was then stirred for 10 min. 50 μL of the solution was deposited on top of the perovskite layer by spincoating at 2000 rpm for 60 s. The sample was purged in N_2 for 30 min. The samples were then exposed for at least one night to ambient conditions in the dark.

5.6. Deposition of the Au electrode

100 nm of Au was deposited with a rate of 1 \AA/s onto the structures in a thermal evaporation chamber at 1×10^{-6} mbar.

5.7. Current density-voltage (J-V) characterization

Current density-voltage (J-V) measurements were performed in an N_2 environment in the dark and under AM 1.5 of sun (100 mW/cm^2) illumination with a LOT solar simulator combined with a Keithley 2400 source meter controlled by a LabView program. We measured at a scan rate of 180 mV/s in reverse scan. Under illumination, an illumination mask was used, and the effective active area was 0.16 cm^2 for these measurements. 21 solar cells (for each device architecture) were measured.

5.8. Impedance spectroscopy

Impedance spectroscopy measurements were performed using a PGSTAT302N (Auto lab, Metrohm) equipped with an impedance analyzer (FRA32M). The frequency range used was 100 kHz–1 Hz, and a AC potential (V_{AC}) amplitude of 10 mV was applied. The employed DC offset was 0.9 V and measurements were performed under AM 1.5 illumination from a solar simulator.

5.9. Operational stability tests under illumination

The operational stability tests were performed under constant AM 1.5 (100 mW/cm^2) illumination of a LOT solar simulator using a Keithley 2400 source meter controlled by a LabView program with the setup at a scan rate of 180 mV/s, where the J-V measurement was started from the initial value of maximum power point (MPP) toward 1.2 V, and then continued in a reverse scan from 1.2 V to -1 V, followed by a forward scan from -1 V to at MPP, after which it was held at this point for ten minutes. The procedure was repeated every 10 min continuously. We extracted the J_0 , R_S , and R_{SH} values shown in Fig. 4 from the J-V curves, which were taken during the stability tests under constant illumination. The R_S and R_{SH} value were extracted from at the 1st, 9th, 19th, 29th, 39th, 49th, 59th, 69th, 79th, 89th and 99th measurement (see in Figure S3a and S3b).

5.10. Photoluminescence spectroscopy

PL measurements on perovskite/ZnO and perovskite/C₆₀/ZnO structures were performed with excitation at 2.64 eV (470 nm) using a Cary Eclipse Varian fluorescence spectrometer with a Xe lamp. The excitation light was rejected using a long-pass filter in the detection path. The measurements were performed under both “front illumination” (with the perovskite layer facing the excitation source) and “back illumination” (with excitation light first passing via the glass/ZnO and the glass/ZnO/C₆₀ layer, and emission collected via the same layer stack).

Author Declaration

All authors have given approval to the final version of the manuscript.

Supplementary Materials

Supplementary material associated with this article can be found, in the online version.

CRediT authorship contribution statement

: Conceptualization, Investigation, Data curation, Writing – original draft. **Loreta A. Muscarella**: Investigation, Writing – original draft. **Yulia Galagan**: Conceptualization, Supervision, Writing – original draft. **Simon Christian Boehme**: Formal analysis, Supervision, Writing – original draft. **Elizabeth von Hauff**: Conceptualization, Formal analysis, Methodology, Supervision, Writing – original draft.

Declaration of Competing Interest

The authors declare that they have no known competing financial interests or personal relationships that could have appeared to influence the work reported in this paper.

Acknowledgment

The Authors thank Damian Glowienka, Isabelli Fabiano, Andreas Peukert and Nadine Tchamba Yimga for assistance with the experiments. Tulus acknowledges the National Research and Innovation Agency (BRIN), the Republic of Indonesia for the scholarship Program for Research and Innovation in Science and Technology (RISET-Pro) World Bank Loan No. 8245-ID. Tulus, Elizabeth von Hauff and Yulia Galagan acknowledge the COST Action Stable Next Generation Photovoltaics (Grant No. MP1307) for support. Yulia Galagan acknowledges the Ministry of Science and Technology of Taiwan (MOST) for supporting the project 110-2222-E-002-001-MY. Simon C. Boehme acknowledges The Netherlands Organization of Scientific Research (NWO) for financial support through the Innovational Research Incentives (Veni) Scheme (Grant No. 722.017.011).

Supplementary materials

Supplementary material associated with this article can be found, in the online version, at doi:10.1016/j.electacta.2022.141215.

References

- [1] A. Kojima, K. Teshima, Y. Shirai, T. Miyasaka, Organometal halide perovskites as visible - light sensitizers for photovoltaic cells, *J. Am. Chem. Soc.* 131 (2009) 6050–6051.
- [2] M.M. Lee, J. Teuscher, T. Miyasaka, T.N. Murakami, H.J. Sanieth, Efficient hybrid solar cells based on meso-superstructured organometal halide perovskites, *Science* 338 (2012) 643–647.
- [3] G. Hodes, Perovskite-based solar cells, *Science* 342 (2013) 317–319.
- [4] W.S. Yang, B.W. Park, E.H. Jung, N.J. Jeon, Y.C. Kim, D.U. Lee, S.S. Shin, J. Seo, E. K. Kim, J.H. Noh, S.I. Seok, Iodide management in formamidinium-lead-

- halide-based perovskite layers for efficient solar cells, *Science* 356 (6345) (2017) 1376–1379.
- [5] M. Saliba, T. Matsui, J.Y. Seo, K. Domanski, J.P. Correa-Baena, M.K. Nazeeruddin, S.M. Zakeeruddin, W. Tress, A. Abate, A. Hagfeldt, M. Grätzel, Cesium-containing triple cation perovskite solar cells: improved stability, reproducibility and high efficiency, *Energy Environ. Sci.* 9 (6) (2016) 1989–1997.
- [6] M. Jeong, I.W. Choi, E.M. Go, Y. Cho, M. Kim, B. Lee, S. Jeong, Y. Jo, H.W. Choi, J. Lee, J.H. Bae, S.K. Kwak, D.S. Kim, C. Yang, Stable perovskite solar cells with efficiency exceeding 24.8% and 0.3-v voltage loss, *Science* 369 (2020) 1615–1620.
- [7] G. Kim, H. Min, K.S. Lee, D.Y. Lee, S.M. Yoon, S.I. Seok, Impact of strain relaxation on performance of α -formamidinium lead iodide perovskite solar cells, *Science* 370 (2020) 108–112.
- [8] X. Li, F. Zhang, H. He, J.J. Berry, K. Zhu, T. Xu, On-device lead sequestration for perovskite solar cells, *Nature* 578 (2020) 555–558.
- [9] M.V. Khenkin, E.A. Katz, A. Abate, G. Bardizza, J.J. Berry, C. Brabec, F. Brunetti, V. Bulović, Q. Burlingame, A. Di Carlo, R. Cheacharoen, Y.B. Cheng, A. Colmann, S. Cros, K. Domanski, M. Duszka, C.J. Fell, S.R. Forrest, Y. Galagan, D. Di Girolamo, M. Grätzel, A. Hagfeldt, Elizabeth von Hauff, H. Hoppe, Jeff Kettle, H. Köbler, M. S. Leite, S. Liu, Y.L. Yueh-Lin Loo, J.M. Luther, C.Q. Ma, M. Madsen, M. Manca, M. Matheron, M. McGehee, R. Meitzner, M.K. Nazeeruddin, A.F. Nogueira, Ç. Odaş, A. Osherov, N.G. Park, M.O. Reese, F.D. Rossi, M. Saliba, U.S. Schubert, H. J. Snaith, S.D. Stranks, W. Tress, P.A. Troshin, V. Turkovic, S. Veenstra, I. Visoly-Fisher, A. Walsh, T. Watson, H. Xi, R. Yildirim, S.M. Zakeeruddin, K. Zhu, M. Lira-Cantu, Consensus statement for stability assessment and reporting for perovskite photovoltaics based on isos procedures, *Nat. Energy* 5 (2020) 35–49.
- [10] E.M. Hutter, T. Kirchartz, B. Ehrler, D. Cahen, E. von Hauff, Pitfalls and prospects of optical spectroscopy to characterize perovskite-transport layer interfaces, *Appl. Phys. Lett.* 116 (2020) 1–7, 100501.
- [11] Q. Cao, Y. Li, H. Zhang, J. Yang, J. Han, T. Xu, S. Wang, Z. Wang, B. Gao, J. Zhao, X. Li, X. Ma, S.M. Zakeeruddin, W.E.I. Sha, X. Li, M. Grätzel, Efficient and stable inverted perovskite solar cells with very high fill factors via incorporation of star-shaped polymer, *Sci. Adv.* 7 (2021) 1–11.
- [12] Z. Dai, S.K. Yadavalli, M. Chen, A. Abbaspourtamijani, Y. Qi, N.P. Padture, Interfacial toughening with self-assembled monolayers enhances perovskite solar cell reliability, *Science* 372 (6542) (2021) 618–622.
- [13] J. Chen, D. He, N.G. Park, Methodologies for >30% efficient perovskite solar cells via enhancement of voltage and fill factor, *Sol. RRL.* 6 (2022) 1–17, 2100767.
- [14] J. Jeong, M. Kim, J. Seo, H. Lu, P. Ahlawat, A. Mishra, Y. Yang, M.A. Hope, F. T. Eickemeyer, M. Kim, Y.J. Yoon, I.W. Choi, B.P. Darwich, S.J. Choi, Y. Jo, J. H. Lee, B. Walker, S.M. Zakeeruddin, L. Emsley, U. Rothlisberger, A. Hagfeldt, D. S. Kim, M. Grätzel, J.Y. Kim, Pseudo-halide anion engineering for α -FAPb₃ perovskite solar cells, *Nature* 592 (2021) 381–385.
- [15] S.H. Turren-Cruz, A. Hagfeldt, M. Saliba, Methylammonium-free, high-performance, and stable perovskite solar cells on a planar architecture, *Science* 362 (2018) 449–453.
- [16] J. Lee, D. Kim, H. Kim, S. Seo, S.M. Cho, N.G. Park, Formamidinium and cesium hybridization for photo- and moisture-stable perovskite solar cell, *Adv. Energy Mater.* 5 (2015), 1501310 (1–9).
- [17] S. Li, K. Fan, Y. Cui, S. Leng, Y. Ying, W. Zou, Z. Liu, C.Z. Li, K. Yao, H. Huang, Unravelling the mechanism of ionic fullerene passivation for efficient and stable methylammonium-free perovskite solar cells, *ACS Energy Lett.* 5 (6) (2020) 2015–2022.
- [18] X.X. Gao, W. Luo, Y. Zhang, R. Hu, B. Zhang, A. Züttel, Y. Feng, M.K. Nazeeruddin, Stable and high efficiency methylammonium free perovskite solar cells, *Adv. Mater.* 32 (2020), 1905502 (1–9).
- [19] W. Qiu, A. Ray, M. Jaysankar, T. Merckx, J.P. Bastos, D. Cheyns, R. Gehlhaar, J. Poortmans, P. Heremans, An interdiffusion method for highly performing cesium /formamidinium double cation perovskites, *Adv. Funct. Mater.* 27 (1700920) (2017) 1–9.
- [20] D.P. McMeekin, G. Sadoughi, W. Rehman, G.E. Eperon, M. Saliba, M.T. Hörlantner, A. Haghghirad, N. Sakai, L. Korte, B. Rech, M.B. Johnston, L.M. Herz, H.J. Snaith, A mixed-cation lead mixed-halide perovskite absorber for tandem solar cells, *Science* 351 (6269) (2016) 151–155.
- [21] R.A.Z. Razera, D.A. Jacobs, F. Fu, P. Fiala, M. Dussouillez, F. Sahli, T.C.J. Yang, L. Ding, A. Walter, A.F. Feil, H.I. Boudinov, S. Nicolay, C. Ballif, Q. Jeangros, Instability of p-i-n perovskite solar cells under reverse bias, *J. Mater. Chem. A* 8 (2020) 242–250.
- [22] S. Mahesh, J.M. Ball, R.D.J. Oliver, D.P. Mcmeekin, B. Johnston, H.J. Snaith, Revealing the origin of voltage loss in mixed-halide perovskite solar cells, *Energy Environ. Sci.* 13 (2020) 258–267.
- [23] J.J. Yoo, G. Seo, M.R. Chua, T.G. Park, Y. Lu, F. Rotermund, Y.K. Kim, C.S. Moon, N.J. Jeon, J.P. Correa-Baena, V. Bulović, S.S. Shin, M.G. Bawendi, J. Seo, Efficient perovskite solar cells via improved carrier management, *Nature* 590 (2) (2021) 587–593.
- [24] Y. Chen, S. Tan, N. Li, B. Huang, X. Niu, Li, Li, M. Sun, Y. Zhang, X. Zhang, C. Zhu, N. Yang, H. Zai, Y. Wu, S. Ma, Y. Bai, Q. Chen, F. Xiao, K. Sun, H. Zhou, Self-elimination of intrinsic defects improves the low-temperature performance of perovskite photovoltaics self-elimination of intrinsic defects improves the low-temperature performance of perovskite photovoltaics, *Joule* 4 (9) (2020) 1961–1976.
- [25] H. Lu, A. Krishna, S.M. Zakeeruddin, M. Grätzel, A. Hagfeldt, Compositional and interface engineering of organic-inorganic lead halide perovskite solar cells, *iScience* 23 (1–14) (2020), 101359.
- [26] P. Zhang, J. Wu, T. Zhang, Y. Wang, D. Liu, H. Chen, L. Ji, C. Liu, W. Ahmad, Z. D. Chen, S. Li, Perovskite solar cells with zno electron - transporting materials, *Adv. Mater.* 30 (1–20) (2018), 1703737.

- [27] G. Yang, H. Tao, P. Qin, W. Ke, G. Fang, Recent progress in electron transport layers for efficient perovskite solar cells, *J. Mater. Chem. A* 4 (11) (2016) 3970–3990.
- [28] Tulus, S. Olthof, M. Marszalek, A. Peukert, L.A. Muscarella, B. Ehrler, O. Vukovic, Y. Galagan, S.C. Boehme, E. von Hauff, Control of surface defects in ZnO nanorod arrays with thermally deposited Au nanoparticles for perovskite photovoltaics, *ACS Appl. Energy Mater.* 2 (5) (2019) 3736–3748.
- [29] B.Q. Zhang, C.S. Dandaneau, X. Zhou, G. Cao, ZnO nanostructures for dye-sensitized solar cells, *Adv. Mater.* 21 (2009) 4087–4108.
- [30] H. Tang, K. Prasad, R. Sanjinés, P.E. Schmid, F. Lévy, Electrical and optical properties of TiO₂ anatase thin films, *J. Appl. Phys.* 75 (1994) 2042–2047.
- [31] J.H. Heo, M.H. Lee, H.J. Han, B.R. Patil, J.S. Yu, S.H. Im, Highly efficient low temperature solution processable planar type CH₃NH₃PbI₃ perovskite flexible solar cells, *J. Mater. Chem. A* 4 (5) (2016) 1572–1578.
- [32] X. Wu, J. Zhang, M. Qin, K. Liu, Z. Lv, Z. Qin, X. Guo, Y. Li, J. Xu, G. Li, H. Yan, X. Lu, ZnO electron transporting layer engineering realized over 20% efficiency and over 1.28 V open-circuit voltage in all-inorganic perovskite solar cells, *EcoMat* e12192 (2022) 1–11.
- [33] J. Yang, B.D. Siempelkamp, E. Mosconi, F.D. Angelis, T.L. Kelly, Origin of the thermal instability in CH₃NH₃PbI₃ thin films deposited on ZnO, *Chem. Mater.* 27 (2015) 4229–4236.
- [34] Y. Cheng, Q.D. Yang, J. Xiao, Q. Xue, H.W. Li, Z. Guan, H.L. Yip, S.W. Tsang, Decomposition of organometal halide perovskite films on zinc oxide nanoparticles, *ACS Appl. Mater. Interfaces* 7 (36) (2015) 19986–19993.
- [35] L.J. Brillson, H.L. Mosbacker, M.J. Hetzer, Y. Strzhemechny, G.H. Jessen, D. C. Look, G. Cantwell, J. Zhang, J.J. Song, Dominant effect of near-interface native point defects on ZnO Schottky barriers, *Appl Phys Lett.* 90 (1-3) (2007), 102116.
- [36] J. Song, L. Liu, X. Wang, G. Chen, W. Tian, T. Miyasaka, Highly efficient and stable low-temperature processed ZnO solar cells with triple cation perovskite absorber, *J. Mater. Chem. A* 5 (2017) 13439–13447.
- [37] L.K. Ono, S.F. Liu, Y. Qi, Reducing detrimental defects for high-performance metal halide perovskite solar cells, *Angew. Chem. Int. Ed.* 59 (2020) 6676–6698.
- [38] C. Liu, W. Wu, D. Zhang, Z. Li, G. Ren, W. Hana, W. Guo, Effective stability enhancement in ZnO-based perovskite solar cells by MAI modification, *J Mater Chem A* 9 (20) (2021) 12161–12168.
- [39] R. Chen, J. Cao, Y. Duan, Y. Hui, T.T. Chuong, D. Ou, F. Han, F. Cheng, X. Huang, B. Wu, N. Zheng, High-efficiency, hysteresis-less, UV-stable perovskite solar cells with cascade ZnO–ZnS electron transport layer, *J. Am. Chem. Soc.* 141 (2019) 541–547.
- [40] L. Meng, F. Zhang, W. Ma, Y. Zhao, P. Zhao, H. Fu, W. Wang, S. Meng, X. Guo, Improving photovoltaic stability and performance of perovskite solar cells by molecular interface engineering, *J. Phys. Chem. C* 123 (2019) 1219–1225.
- [41] K. Yao, X. Wang, Y. Xu, F. Li, L. Zhou, Multilayered perovskite materials based on polymeric-ammonium cations for stable large-area solar cell, *Chem. Mater.* 28 (2016) 3131–3138.
- [42] N.K. Noel, A. Abate, S.D. Stranks, E.S. Parrott, V.M. Burlakov, A. Goriely, H. J. Snaith, Enhanced photoluminescence and solar cell performance via Lewis base passivation of organic to inorganic lead halide perovskites, *ACS. Nano* 8 (10) (2014) 9815–9821.
- [43] D.H. Sin, S.B. Jo, S.G. Lee, H. Ko, M. Kim, H. Lee, K. Cho, Enhancing the durability and carrier selectivity of perovskite solar cells using a blend interlayer, *ACS Appl. Mater. Interfaces* 9 (21) (2017) 18103–18112.
- [44] G. Hyun, S. Park, J. Jeong, K.S. Lee, D.I. Son, H. Lee, Y. Yi, Unveiling the electronic structure of ZnO–C₆₀ core-shell quantum dots: the origin of efficient electron transport, *J. Phys. Chem. C* 121 (2017) 12230–12235.
- [45] K. Wojciechowski, T. Leijtens, S. Siprova, C. Schlueter, M.T. Ho, J.T. Wang, C. Li, A. K. Jen, T. Lee, H.J. Snaith, C₆₀ as an efficient n-type compact layer in perovskite solar cells, *J. Phys. Chem. Lett.* 6 (2015) 2399–2405.
- [46] D. Liu, Q. Wang, C.J. Traverse, C. Yang, M. Young, P.S. Kuttipillai, S.Y. Lunt, T. W. Hamann, R.R. Lunt, Impact of ultrathin C₆₀ on perovskite photovoltaic devices, *ACS Nano* 12 (2018) 876–883.
- [47] X. Liu, Z. Liu, H. Ye, Y. Tu, B. Sun, X. Tan, T. Shi, Z. Tang, Novel efficient C₆₀ based inverted perovskite solar cells with negligible hysteresis, *Electrochim. Acta* 288 (2018) 115–125.
- [48] N. Klipfel, A.O. Alvarez, H. Kanda, A.A. Sutanto, C. Igci, C. Roldán-Carmona, C. Mombiona, F. Fabregat-Santiago, M.K. Nazeeruddin, C₆₀ thin films in perovskite solar cells: efficient or limiting charge transport layer? *ACS. Appl. Energy Mater.* 5 (2022) 1646–1655.
- [49] E. von Hauff, Impedance spectroscopy for emerging photovoltaics published as part of the journal of physical chemistry virtual special issue “young scientists, *J. Phys. Chem. C* 123 (2019) 11329–11346.
- [50] B.A. Boukamp, A linear Kronig-Kramers transform test for admittance data validation, *J. Electrochem. Soc.* 142 (6) (1995) 1885–1894.
- [51] M. Schönleber, D. Klotz, E. Ivers-Tiffée, A method for improving the robustness of linear Kronig-Kramers validity tests, *Electrochim Acta* 131 (2014) 20–27.
- [52] M. Schönleber, E. Ivers-Tiffée, Approximability of impedance spectra by RC elements and implications for impedance analysis, *Electrochem. Commun.* 58 (2015) 15–19.
- [53] E. von Hauff, D. Klotz, Impedance spectroscopy for perovskite solar cells: characterisation, analysis, and diagnosis, *J. Mater. Chem. C* 10 (2) (2022) 742–761.
- [54] D. Klotz, G. Tumen-ulzii, C. Qin, T. Matsushima, C. Adachi, Detecting and identifying reversible changes in perovskite solar cells by electrochemical impedance spectroscopy, *RSC Adv* 9 (2019) 33436–33445.
- [55] D. Klotz, Negative capacitance or inductive loop? A general assessment of a common low frequency impedance feature, *Electrochem. Commun.* 98 (11) (2019) 58–62.
- [56] A. Peukert, L.V. Roca, M. Scherer, R. Lovrincic, C. Ramanan, A. Chanaewa, E. von Hauff, Controlled morphology of ZnO nanorods for electron transport in squaraine bulk-hetero junction solar cells with thick active layers, *Sol. Rrl.* 1 (12) (2017), 1700132.
- [57] B.W. Park, N. Kedem, M. Kulbak, D.Y. Lee, W.S. Yang, N.J. Jeon, J. Seo, G. Kim, K. J. Kim, T.J. Shin, G. Hodes, D. Cahen, S.I. Seok, Understanding how excess lead iodide precursor improves halide perovskite solar cell performance, *Nat. Commun.* 9 (1-8) (2018) 3301.
- [58] P. Hang, J. Xie, C. Kan, B. Li, Y. Zhang, P. Gao, D. Yang, X. Yu, Stabilizing fullerene for burn-in-free and stable perovskite solar cells under ultraviolet preconditioning and light soaking, *Adv. Mater.* 33 (1-9) (2021), 2006910.
- [59] S. Paek, S.B. Khan, M. Franckevicius, R. Gegevičius, O.A. Syzgantseva, M. A. Syzgantseva, S. Kinche, A.M. Asiri, C. Roldan-Carmona, M.K. Nazeeruddin, Cation optimization for burn-in loss-free perovskite solar devices, *J. Mater. Chem. A* 9 (2021) 5374–5380.
- [60] S.G. Motti, J.B. Patel, R.D.J. Oliver, H.J. Snaith, M.B. Johnston, L.M. Herz, Phase Segregation in mixed-halide perovskites affects charge-carrier dynamics while preserving mobility, *Nature Commun.* 12 (1-9) (2021) 6955.
- [61] A.J. Knight, J. Borchert, R.D.J. Oliver, J.B. Patel, P.G. Radaelli, H.J. Snaith, M. B. Johnston, L.M. Herz, Halide segregation in mixed-halide perovskites: influence of a-site cations, *ACS Energy Lett.* 6 (2021) 799–808.
- [62] L. Hu, X. Guan, W. Chen, Y. Yao, T. Wan, C.H. Lin, N.D. Pham, L. Yuan, X. Geng, F. Wang, C.Y. Huang, J. Yuan, S. Cheong, R.D. Tilley, X. Wen, D. Chu, S. Huang, T. Wu, Linking phase segregation and photovoltaic performance of mixed-halide perovskite films through grain size engineering, *ACS Energy Lett.* 6 (2021) 1649–1658.
- [63] A.A. Zhumekenov, M.I. Saidaminov, M.A. Haque, E. Alarousi, S.P. Sarmah, B. Murali, I. Dursun, X.H. Miao, A.L. Abdelhady, T. Wu, O.F. Mohammed, O. M. Bakr, Formamidinium lead halide perovskite crystals with unprecedented long carrier dynamics and diffusion length, *ACS Energy Lett.* 1 (2016) 32–37.
- [64] Y. Sun, J. Peng, Y. Chen, Y. Yao, Z. Liang, Triple-cation mixed-halide perovskites: towards efficient, annealing-free and air-stable solar cells enabled by Pb(SCN)₂, *Additive. Sci Rep.* 7 (1-7) (2017) 46193.
- [65] E.T. Hoke, D.J. Slotcavage, E.R. Dohner, A.R. Bowring, H.I. Karunadasa, M. D. McGehee, Reversible photo-induced trap formation in mixed-halide hybrid perovskites for photovoltaics, *Chem. Sci.* 6 (2015) 613–617.